PAPER • OPEN ACCESS

Fluid demixing kinetics on spherical geometry: power spectrum and Minkowski functional analysis

New Journal of Physics
The open access journal at the forefront of physics

Deutsche Physikalische Gesellschaft DPG
IOP Institute of Physics

Published in partnership with: Deutsche Physikalische Gesellschaft and the Institute of Physics

OPEN ACCESS

RECEIVED
4 October 2018

REVISED
30 November 2018

ACCEPTED FOR PUBLICATION
17 December 2018

PUBLISHED
30 January 2019

PAPER

Fluid demixing kinetics on spherical geometry: power spectrum and Minkowski functional analysis

A Böbel[1], M C Bott[2], H Modest[1], J M Brader[2] and C Räth[1]

[1] Institut für Materialphysik im Weltraum, Deutsches Zentrum für Luft- und Raumfahrt (DLR), Münchener Str. 20, D-82234, Weßling, Germany
[2] Soft Matter Theory, University of Fribourg, Switzerland

E-mail: alexander.boebel@dlr.de

Keywords: morphological data analysis, demixing, curved space, spinodal decomposition

Supplementary material for this article is available online

Abstract

Dynamic density functional theory calculations of fluid–fluid demixing on spherical geometries are characterized via their angular power spectrum as well as via the Minkowski functionals (MFs) of their binarized fluid density fields. MFs form a complete set of additive, motion invariant and continuous morphological measures sensitive to nonlinear (spatial) correlations. The temporal evolution of the fluid density fields is analyzed for different sphere sizes and mixing compositions. The demixing process in the stages of early spinodal decomposition and consecutive domain growth can be characterized by both methods and a power-law domain growth $L(t) \propto t^{\alpha}$ is evidenced for the MF measures. The average domain size obtained by the structure factor only responds to the late stage domain growth of the demixing process. MFs provide refined insights into the demixing process: they allow the detection of distinct stages in the early spinodal decomposition, provide a precise measure of the relative species composition of the mixture and, most importantly: after a proper rescaling, they allow the detection of a universal demixing behavior for a wide range of mixture fractions and for different sphere sizes.

1. Introduction

If a binary fluid mixture is in the immiscible state it will start to dynamically demix in order to reach the thermodynamically stable state of two coexisting phases. This phase separation can be split in two consecutive regimes [1–3]: the spinodal decomposition in the early stage, followed by the domain growth stage. During spinodal decomposition fluid density fluctuations increase exponentially and neighboring particles agglomerate to form disjoint domains. In the domain growth stage the size of these initial domains increases further and they start to coalesce with neighboring domains in order to reduce the energy costs of the interface areas. As the domain morphology is preserved, this domain growth is self-similar in time. The self-similarity implies a time-dependent characteristic length of the mean domain size that can be described by a power-law growth $L(t) \propto t^{\alpha}$.

When the system is spatially confined, the phase separation kinetics are less well understood. Spatial confinement can be imposed by obstacles and external fields [4, 5]. Another form of spatial confinement can be achieved via the geometry of space itself [6]. Recently, the study of statistical physics processes on curved surfaces, in particular on the sphere, has attracted growing interest and showed the richness of physical phenomena that are influenced by their embedding on non-flat geometries. The crystallization of a colloidal suspension on a sphere was explained via a icosahedrically symmetric order parameter that revealed the long-range order of the crystal on the curved surface [7]. The projection of inhomogeneous crystals onto homogeneous ones on curved surfaces enabled the prediction of defect distributions [8]. Also, unusual emergent structures due to advection were demonstrated on a spherical geometry [9].

Common methods for the characterization of demixing dynamics are based on linear measures: the mean domain size is measured via the first zero crossing of the radial correlation function or equivalently via the first maximum of the power spectral structure factor [10–12]. However, this method is computationally expensive [13]. Another drawback lies in the linearity of the method. The mean domain size is not a sufficient descriptor of the domain morphology [3, 14, 15]. Thus, it is beneficial to extend the description of the demixing system to morphological measures, which are sensitive to higher order correlations.

Morphological measures that capture the complete nonlinear structural information of a system are the Minkowski functionals (MFs) [16]. They became a prominent tool for morphological data analysis since they form a complete family of structural descriptors sensitive to nonlinear properties. MFs are well suited for the investigation of demixing processes [3, 14, 15] and can readily be applied on spherical geometry [17–19]. In two-dimensional flat and curved spaces the MFs are easily interpretable measures connected to concepts as area, perimeter and the Euler characteristic. The Euler characteristic is a measure for the connectivity of a spatial structure.

In this work we aim to systematically study the properties of dynamic density functional theory calculations (DDFT) of fluid demixing on a spherical geometry with both linear and nonlinear measures. The DDFT calculations were already utilized as the basis for the studies in [6] and are reused here as a convenient starting point for the first ever MF analysis of fluid–fluid demixing on spherical geometries. Initially we apply the conventional linear method known in the flat space case to the spherical data: we calculate the angular power spectral density and fit it to a general structure factor function in order to calculate the average domain size L. These results are then compared with the MF measures.

This paper is structured as follows: in section 2 we explain the methods and results for the calculation of the phase separation dynamics on the spherical body. Section 3 describes the method of the structure factor calculation based on the angular power spectral density and the implementation of the MF calculation. The results of power spectral density and MF analysis for DDFT calculations with different sphere sizes and mixture parameters are presented in section 4. Finally, in section 5 results are discussed and conclusions drawn.

2. Dynamic density functional theory calculations

This section is intended to give a brief overview of the methods and results found about phase separation on a large spherical particle [6]. The data for the evolution of the density distribution during spinodal decomposition forms the basis for the MF analysis discussed in this manuscript.

In order to avoid any confusion with terminology, we will henceforth refer to the large particle as the 'meso-particle' and the smaller, mobile particles constituting the fluid on its surface as the 'surface particles'.

2.1. The Gaussian core model (GCM)

To represent the surface particles, we consider a model binary mixture, thus two particle species, in which the particles interact via the soft repulsive pair potential

$$\beta v_{ij}(r) = \beta\epsilon_{ij} \exp\{-r^2/R_{ij}^2\}. \tag{1}$$

Here the non-negative parameters ϵ_{ij}, R_{ij} and $\beta = (k_B T)^{-1}$ determine the strength and range, respectively, of the interaction between species i and j. The GCM was introduced by Stillinger [20] to study phase separation in binary mixtures and has since been studied intensively, both in bulk and at interfaces [21]. The model has the advantage that a simple mean-field approximation to the free energy provides good agreement with computer simulation data [22] and is therefore straight forward to incorporate in a density functional theory.

2.2. Mean-field free energy functional

To describe the collective behavior of the surface particles we use an approximation to the two-dimensional Helmholtz free energy functional

$$\begin{aligned}\beta\mathcal{F}[\{\rho_i(\mathbf{r})\}] = &\sum_i \int \mathrm{d}\mathbf{r}\rho_i(\mathbf{r})(\ln(\rho_i(\mathbf{r})) - 1) \\ &+ \frac{1}{2}\sum_{ij}\int \mathrm{d}\mathbf{r}\int \mathrm{d}\mathbf{r}'\rho_i(\mathbf{r})\rho_j(\mathbf{r}')\beta v_{ij}(|\mathbf{r}-\mathbf{r}'|),\end{aligned} \tag{2}$$

where the first and second terms provide the ideal and excess (over ideal, describing the particle interactions) contributions, respectively. The subscripts i and j are species labels and the notation $[\{\rho_i(\mathbf{r})\}]$ indicates a functional dependence on the one-body density profiles of all species. We set the (physically irrelevant) thermal wavelength λ equal to unity. For a binary mixture the species indicies are restricted to the values $i, j = 1, 2$.

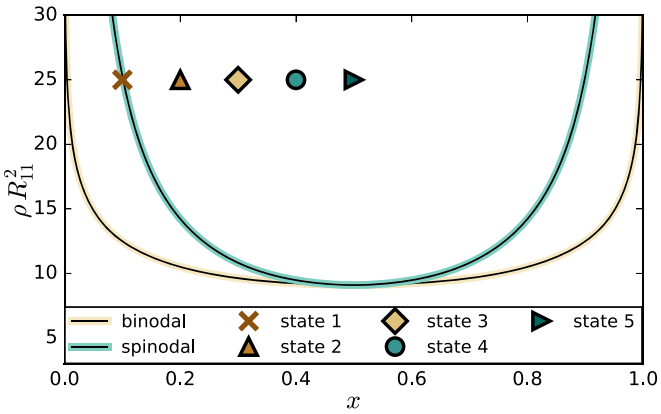

Figure 1. Phase diagram for the planar system as a reference point. Binodal and spinodal curves, as well as the states analyzed in this study are indicated. The states are $x \in \{0.1,\ 0.2,\ 0.3,\ 0.4,\ 0.5\}$ for $\rho R_{11}^2 = 25$. Parameters are $R_{11} = R_{22} = R_{12} = 1$, $\epsilon_{11}^* = \epsilon_{22}^* = 1$, $\epsilon_{12}^* = 1.035\epsilon_{11}^*$. The critical point is found at $\rho R_{11}^2 = 9.094\ 568$ and $x = 0.5$.

In bulk, the number density of species i is $\rho_i = N_i/V$, where V is the area in the 2d case and N_i the number of particles of species i. The total density is of the surface particles $\rho = \rho_1 + \rho_2$.

It is convenient to introduce a concentration variable, the mixture parameter $x = N_2/N$, with the total number of particles N. This enables the species labeled densities to be expressed as $\rho_1 = (1-x)\rho$ and $\rho_2 = x\rho$. In these variables the bulk free energy per particle consists of a sum of two terms, $f \equiv F/N = f_{\mathrm{id}} + f_{\mathrm{ex}}$. The ideal part is given by

$$\beta f_{\mathrm{id}} = \ln(\rho) - 1 + (1 - x)\ln(1 - x) + x\ln(x), \tag{3}$$

and the reduced bulk excess free energy per particle can be written as

$$\beta f_{\mathrm{ex}} = \frac{1}{2\rho}(\rho_1\rho_1\hat{v}_{11} + 2\rho_1\rho_2\hat{v}_{12} + \rho_2\rho_2\hat{v}_{22}). \tag{4}$$

where $\hat{v}_{ij} = \epsilon_{ij}^* R_{ij}^2 \pi$ and $\epsilon_{ij}^* = \beta\epsilon_{ij}$. In [6] the parameters $R_{11} = R_{22} = R_{12} = 1$, $\epsilon_{11}^* = \epsilon_{22}^* = 2$ and $\epsilon_{12}^* = 1.035\epsilon_{11}^*$ where chosen and the phase diagram for an infinite planar system has been calculated. This phase diagram is shown in figure 1 and indicates the five states that will be analyzed in this study for a large $R = 10R_{11}$, respectively a small $R = 2.5R_{11}$ sphere. Even though the meso-sphere represents a finite size system the phase diagram for the bulk system offers a useful guide. When the total density ρ becomes sufficiently large the GCM demixes.

2.3. Dynamical density functional theory and numerical implementation

To study phase separation on the surface of a meso-particle we will focus on the dynamics of the one-body density of the surface particles. This can be obtained using DDFT [23, 24]. Within this approach the time evolution of the density of species i is given by a

$$\gamma^{-1}\frac{\partial\rho_i(\mathbf{r},\ t)}{\partial t} = \frac{\partial}{\partial\mathbf{r}}\cdot\left[\rho_i(\mathbf{r},\ t)\frac{\partial}{\partial\mathbf{r}}\frac{\delta\mathcal{F}[\{\rho_i(\mathbf{r},\ t)\}]}{\delta\rho_i(\mathbf{r},\ t)}\right]. \tag{5}$$

Here γ is the mobility and it is related to the diffusion coefficients D as $\gamma = \beta D$. The DDFT equation of motion (5) is a generalized diffusion equation. The one-body density is driven by gradients in the local chemical potential which arise from the particle interaction described by the functional for the free energy (2). If we insert the functional of the ideal gas, we recover the well known diffusion equation for a non interacting gas.

To solve the DDFT equation of motion (5) on the surface of a meso-sphere we chose to parametrize the sphere using the spherical polar angles θ and ϕ. With this approach we have an accurate finite-difference scheme for calculating the gradient and divergence of scalar- and vector fields. In addition we make use of the convolution theorem on the unit-sphere [6, 25] to efficiently compute the convolution of two scalar fields in the space of spherical harmonic functions. The numerical methods for solving equation (5) on the surface of a sphere are described in more detail in [6].

2.4. DDFT calculation results

For larger meso-sphere radii ($R = 10R_{11}$) we find standard spinodal decomposition dynamics for an equal mixture, $x = 0.5$, leading to a 'half–half' final state. As the value of x is reduced towards the spinodal, then the

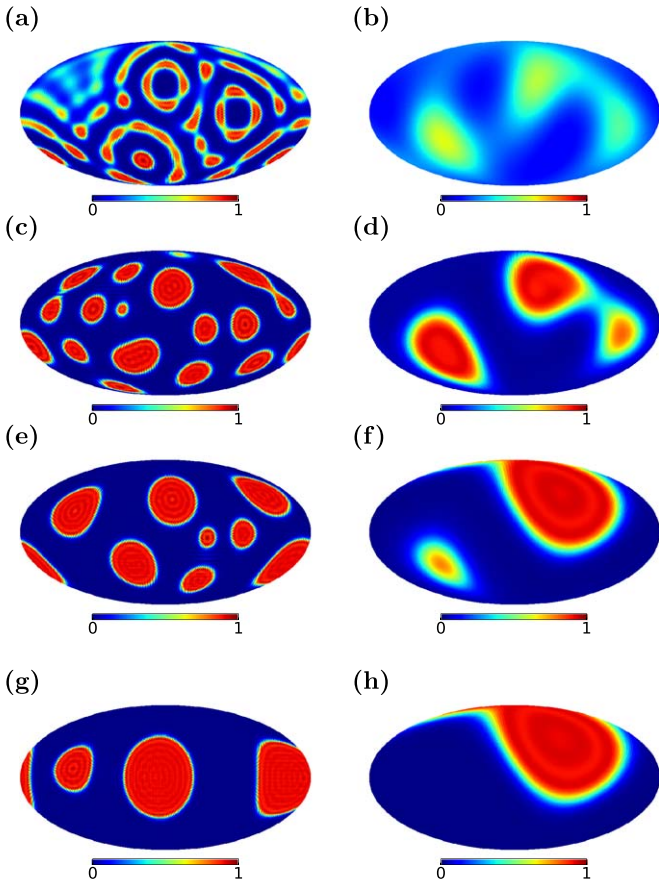

Figure 2. Mollweide projection of equal area pixelisation for the DDFT calculation data for $x = 0.3$. Left column: (a), (c), (e), (g) Evolution of the particle density $\rho_2(\mathbf{r}, t^*)$ of species two for the large sphere $R = 10R_{11}$. Right column: (b), (d), (f), (h) Evolution of the particle density for the small sphere $R = 2.5R_{11}$.

phase separation dynamics are given by the Ostwald ripening scenario [26], where islands of the minority phase form, which then slowly merge together (see figure 2). For the phase separation on the smaller meso-particle ($R = 2.5R_{11}$) finite-size effects become more important. In contrast to the behavior on the larger meso-sphere, the density evolves here in most cases into a 'band' state, where two islands with species 1 form, separated by a band of species 2 particles. This state is stable over a long time. The smaller we chose the mixture parameter x the longer the metastable band state lives. This enhanced stability of the band structure can be attributed to the fact that the distance between the interfaces increases as the surface coverage of the minority phase is reduced by reducing x. In the following analyses we only consider one of the species and call its density field $\rho_2(\mathbf{r}, t^*) \equiv \rho(\mathbf{r}, t^*)$. Since their contributions are mirror images their information content is redundant. t^* is the dimensionless time given by $t^* = tD/R_{11}^2$, where D is the bare diffusion coefficient.

Movies for all DDFT calculations are provided in the supplemental material available online at stacks.iop.org/NJP/21/013031/mmedia.

2.5. Equal area pixelisation

Using the python library healpy [27] for HEALPix the spherical coordinate grid ($181 \times 92 = 16652$ pixel) was interpolated on a equal area pixel grid with $N_{\mathrm{pix}} = 12\,288$ pixel in order to apply the MF analysis straightforwardly. The HEALPix pixelisation scheme is a partition of a spherical surface into exactly equal area quadrilateral pixels of varying shape [28] but uniform area A_{pix}. The pixel size depends on the HEALPix resolution parameter of the grid equal to $N_{\mathrm{side}} = 1, 2, 4, 8, \ldots$ corresponding to a total number of pixels of $N_{\mathrm{pix}} = 12 \times N_{\mathrm{side}}^2 = 12, 48, 192, 768, \ldots$ In this work we use a resolution parameter of $N_{\mathrm{side}} = 32$, since this is the closest match to the raw data in the spherical coordinate grid. In further studies much higher resolutions can be obtained. In figure 2 the pixelization of the density fields $\rho(\mathbf{r}, t^*)$ is shown for both sphere sizes during the evolution of time t^*.

3. Spatial statistics

3.1. Angular power spectral density

Any scalar function $\rho(\mathbf{n})$ on a spherical geometry, where $\mathbf{n}(\theta,\ \phi)$ is a direction on the sphere, can be decomposed into its spherical harmonics representation. The spherical harmonics Y_{lm} form an orthonormal base on the unit sphere. They are given by:

$$Y_{lm} = \sqrt{\frac{2l+1}{4\pi}\frac{(l-m)!}{(l+m)!}}P_l^m(\cos(\theta))\mathrm{e}^{\mathrm{i}m\phi}. \tag{6}$$

With indices $l \in \mathcal{N}_0$ and $-l \leqslant m \leqslant l$. P_l^m are the Legendre polynomials. l is the multipole. The average solid angle Ω corresponding to a specific l is $\Omega = 4\pi/2l$. Considering the division of the sphere in $2l$ equal slices, the widest part of these slices corresponds to an angle $\gamma = \pi/l$. This translates into a length scale $L = R \cdot \pi/l$, with the sphere radius R.

Then $\rho(\mathbf{n})$ can be expanded as:

$$\rho(\mathbf{n}) = \sum_{l\geqslant 0}\sum_{|m|\leqslant l} a_{lm}Y_{lm}(\mathbf{n}), \tag{7}$$

with harmonic coefficients a_{lm} given by the projection

$$a_{lm} = \int \mathrm{d}\Omega\ \rho(\mathbf{n})\,Y_{lm}^*(\mathbf{n}). \tag{8}$$

$\circ^*$ denotes the complex conjugate of $\circ$. The power spectrum C_l of the scalar field $\rho(\mathbf{n})$ can be defined as the variance of the harmonic coefficients $\langle a_{lm}a_{l'm'}^*\rangle = \delta_{ll'}\delta_{mm'}C_l$ with

$$C_l = \frac{1}{2l+1}\sum_{|m|\leqslant l}\langle |a_{lm}|^2\rangle. \tag{9}$$

The C_l are called the angular power spectral density. Since for any l there exist $2l+1$ modes of m the total power for the multipole l is given by $(2l+1)\cdot C_l$.

In the following we analyze the position $l_{\max}$ and value $C_{l,\max}$ of the maximum of the power spectral density. $l_{\max}$ is a measure for the length scale of the most dominant pattern. This quantity is the standard metric to characterize the domain growth of demixing processes [2, 3, 12, 13, 29]. Here we also introduce the power $C_{l,\max}$ as a measure for the domain growth. $C_{l,\max}$ is a measure for the dominance of the most predominant pattern (in terms of spherical harmonics) of the function on the sphere.

The position of the maximum is determined, using the standard procedure, via fitting the off-critical fitting function $S(l,\ t) \propto (l\cdot L_{\mathrm{PS}}(t)/2\pi)^2/[2+(l\cdot L_{\mathrm{PS}}(t)/2\pi)^6]$ [30] and the average domain size L_{PS} is identified as $R\pi/l_{\max}$.

3.2. Minkowski functionals

Since the early 20th century [16] MFs have been known in integral geometry [31, 32] and became a prominent tool for morphological data analysis [33]. They are able to characterize the geometry and shape of structural data as well as their topology and connectedness. MFs are sensitive to any n-point correlation function and thus can provide new insights into physical processes beyond the capability of linear methods, e.g. power spectral density measures.

On the two-dimensional sphere $\mathcal{S}^2$ with radius R in $D = 2$ dimensions the $D+1$ MFs M_ν, $\nu \in \{0,\ 1,\ 2\}$ for a set $K \subseteq \mathcal{S}^2$ are the area M_0, the perimeter M_1 and the Euler characteristic M_2. They are defined as:

$$\begin{aligned} M_0(K) &= \int_K \mathrm{d}^2r \\ M_1(K) &= \frac{1}{4}\int_{\partial K}\mathrm{d}r \\ M_2(K) &= \frac{1}{2\pi}\int_{\partial K}\kappa(r)\ \mathrm{d}r. \end{aligned} \tag{10}$$

Here, $\kappa(r)$ is the local Gaussian curvature.

MFs are motion invariant, additive and conditionally continuous. They form a complete family of morphological measures. Or vice versa: Any motion invariant, conditionally continuous and additive functional is a superposition of the countably many MFs [34]. They are nonlinear measures sensitive to any higher order correlations. They are homogeneous functions of order $D-\nu$:

$$M_\nu(\lambda K) = \lambda^{D-\nu}M_\nu(K). \tag{11}$$

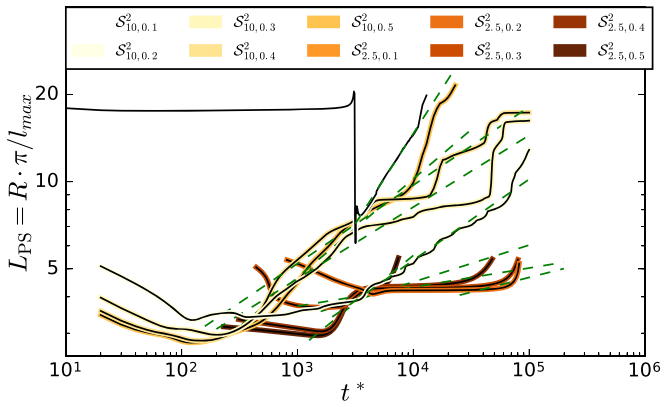

Figure 3. Power spectrum analysis: The characteristic length scale $L_{PS} = R\pi/l_{max}$ is identified via the position of the maximum of the angular power spectrum $l_{max} = l|_{C_l = C_{l,max}}$. It is the standard measure for the average domain size. Different sphere radii R and mixture parameters x are color coded. Their values are indicated in the legend by $\mathcal{S}^2_{R/R^2_{\Pi},x}$. $\mathcal{S}^2$ denotes the two-dimensional sphere. As a guide to the eye power-law fits are presented as green dashes lines. The signal for $\mathcal{S}^2_{2.5,0.1}$ is not shown. It is very small since no demixing occurs during the calculation time.

There is a broad range of applications of MFs, e.g. curvature energy of membranes [35], order parameter in Turing patterns [36], density functional theory for fluids (as hard balls or ellipsoids) [37, 38], testing point distributions (find clusters, filaments, underlying point-process) or searching for non-Gaussian signatures in the cosmic microwave background [17–19, 39, 40].

In order to study the morphology of the smooth, scalar density fields $\rho(\mathbf{r}, t^*)$, the MFs of the excursion sets K_{th} of the equal area pixelization of the simulation data are calculated. K_{th} is the set of all pixels with density values $\rho(\mathbf{r}, t^*)$ that are higher or at least equal to a threshold value ρ_{th}: $K_{th} = \{\mathbf{r} \in \mathcal{S}^2 | \rho(\mathbf{r}, t^*) \geqslant \rho_{th}\}$. These pixels mark the regions $\mathbf{r}$ on $\mathcal{S}^2$ that have a density $\rho(\mathbf{r}, t^*)$ greater or equal to the threshold density ρ_{th}, at the time t^*.

By running over 101 equidistant threshold steps $\rho_{th,k}$ (with $k \in \{0, \ldots, 100\}$) the density fields are binarized into an active and a non-active part. The first threshold step $\rho_{th,0}$ is chosen such that every pixel on $\mathcal{S}^2$ is active. The last step $\rho_{th,100}$ is reached when all pixels are excluded and inactive.

For the implementation of the explicit calculation the algorithm proposed in [41] is adapted to compute MFs of pixelized maps: due to the additivity of the MFs the calculation can be performed by the summation of local contributions. Individual pixels are considered to be composed of 4 vertices, 4 edges and their interior area. The total number of active pixels n_s, the number of edges n_e and vertices n_v at the interface of active and inactive pixels is counted. Then the area M_0, the integral mean curvature (or perimeter) M_1 and the Euler characteristic M_2 can be calculated as sums:

$$\begin{aligned} M_0 &= n_s \\ M_1 &= -4n_s + 2n_e \\ M_2 &= n_s - n_e + n_v. \end{aligned}$$

In order to avoid any double counting of edges or vertices the original field is built up iteratively by adding active pixels to the initially empty temporary field individually. Only if all neighboring pixels have already been built into the temporary field the edges and vertices are added to the total sum. The number of arithmetic operations required to compute the MFs scales linearly with the number of active pixels and the total number of pixels of the image.

4. Results

4.1. Power spectral density

The angular power spectral densities obtained for the DDFT calculations on different sphere sizes R and with different mixture parameters x are presented in the supplementary material.

The graphs for the average domain size, measured as the characteristic length scale $L_{PS} = R\pi/l_{max}$, derived from the positions of maximal power spectrum amplitudes l_{max} are presented in figure 3. In these graphs the initial spinodal decomposition phase of nucleation cannot be observed. L_{PS} is blind for the initial demixing stage (exponential growth of density fluctuations) where yet no domain growth can be observed. However, in the coalescence stage, an increase of L_{PS} is found that can be fitted to a power-law. The power law is better reproduced in the large sphere graphs, since they allow for more individual domains, more coalescence events

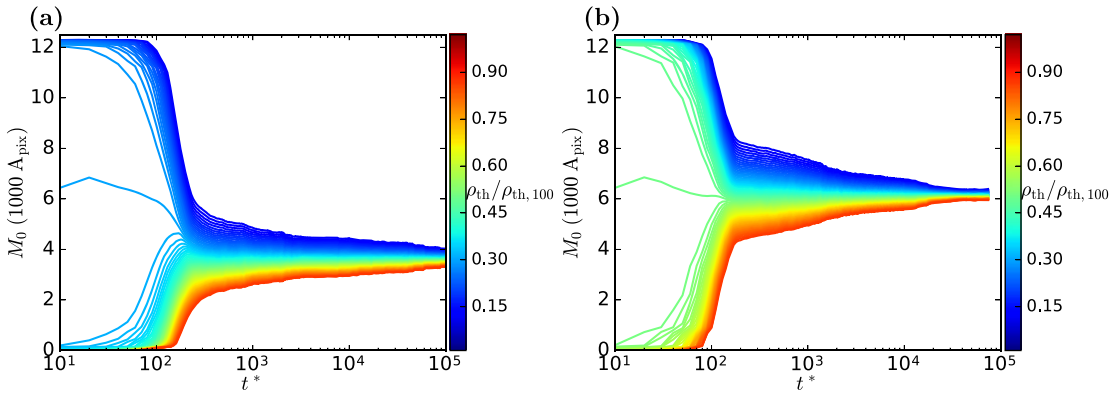

Figure 4. Area Minkowski functional M_0, dependent on the relative threshold density $\rho_{th}/\rho_{th,100}$, for large sphere $R = 10R_{11}$. Threshold values $\rho_{th}/\rho_{th,100}$ are color coded. (a) $x = 0.3$, (b) $x = 0.5$.

and therefore provide a more constant slope in the log–log plot. The small sphere graphs show plateaus between power law growth. During plateau phases no coalescence of domains happens because of the low number of individual domains on the small sphere. The onset of demixing is much later for the small sphere compared to the large sphere. Also smaller mixture parameters correlate with later times for the onset of demixing. In particular for $R = 2.5R_{11}$ and $x = 0.1$ no demixing is observed during the complete DDFT calculation, ending at $t^* = 10^5$. The domain growth is faster for higher mixture parameters, the exception being $x = 0.1$: here the demixing processes starts late but domain growth is fast.

4.2. Minkowski functionals

The dependence of the MFs on the threshold density ρ_{th} is presented in the supplementary material.

The temporal evolution of the MFs is also presented in the supplementary material. Here two plots are shown representatively: figure 4 shows the area functional M_0 for the mixing fractions $x = 0.3$ in panel (a) and $x = 0.5$ in panel (b). The relative threshold value $\rho_{th}/\rho_{th,100}$ is color coded. For early times there is a qualitative difference for the regimes $\rho_{th}/\rho_{th,100} < x$ and $\rho_{th}/\rho_{th,100} > x$ for M_0. (Also $M_1(\rho_{th})$ and $M_2(\rho_{th})$ have a higher variance in the early time phase during spinodal decomposition. See supplementary material.) The functional at the crossover value $\rho_{th}/\rho_{th,100} \simeq x$ deviate significantly from the functional values at neighboring threshold values. Any other threshold variations only show small changes in the shape of the curve. In the initial mixture the density is $\rho/\rho_{th,100} \simeq x$, all relative threshold values below x result in almost no active pixels after binarization, but most pixels are active for higher thresholds. This leads to a sharp transition of the MFs from detecting almost all pixels as active to detecting almost no active pixels at $\rho_{th}/\rho_{th,100} \simeq x$. Thus it is easy to detect the composition parameter x via the shape of MF curves even only analyzing the initial phase of spinodal decomposition.

After a certain point in time, however, the curves are essentially the same. This point can be identified as the time t_c^* where the spinodal decomposition transitions from the early nucleation stage to the late stage coalescence regime. With these curves t_c^* can easily be determined. In particular using non-morphological measures like e.g. the correlation function the determination of t_c^* proves to be more difficult and computationally expensive [13].

The MF graphs obtained on the sphere are in qualitative agreement with MF calculated for spinodal decomposition in flat two-dimensional geometry [14, 15].

4.3. Stages during spinodal decomposition

In the following analysis a specific threshold value ρ_{th} is chosen for any DDFT calculation. It is choosen such that the minimal detected number of active pixels is close to 1. (This happens at $\rho_{th}/\rho_{th,100} \simeq x$.) Then the MFs have a maximal dynamic range. These MF graphs are presented, for the area functional M_0, in figure 5. In all functional graphs both, the spinodal decomposition and the subsequent coalescence stage of demixing can be evidenced. During spinodal decomposition the M_0 area functional follows a power law. In the coalescence stage it assumes a constant value since the individual domains only grow by merging with neighboring domains. M_1 also grows fast during spinodal decomposition. However, during the coalescence stage it drops again, thus providing a means to easily determine the crossover time t_c^*. (Compare figure 6, or consult the supplementary material.) We obtain $t_c^* \simeq 2 \times 10^2$ in the case of $R = 10R_{11}$ and $t_c^* \simeq 2 \times 10^3$ in the case of $R = 2.5R_{11}$.

A difference in the shape of the graphs for the large and small sphere can be observed: in the large sphere graphs M_0 has a small, non-vanishing slope before the main growth phase evidences the initial nucleation. This

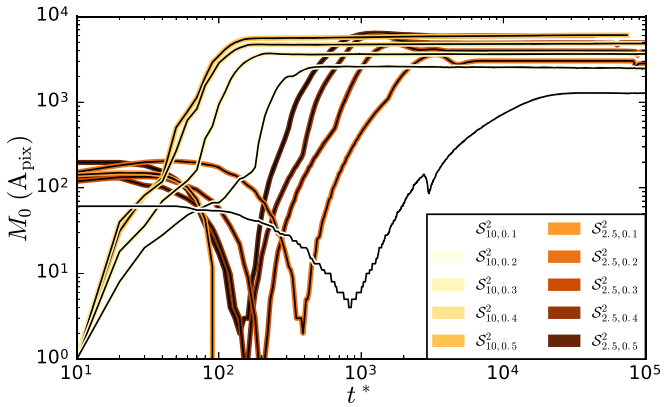

Figure 5. Area Minkowski functional M_0 for threshold values $\rho_{\mathrm{th}}/\rho_{\mathrm{th},100} \simeq x$. Exact threshold values are $\rho_{\mathrm{th}}/\rho_{\mathrm{th},100} \in [0.134,\ 0.212,\ 0.316,\ 0.416,\ 0.515\ 4]$. Different sphere radii R and mixture parameters x are color coded. Their values are indicated in the legend by $\mathcal{S}^2_{R/R^2_{\square},x}$. $\mathcal{S}^2$ denotes the two-dimensional sphere.

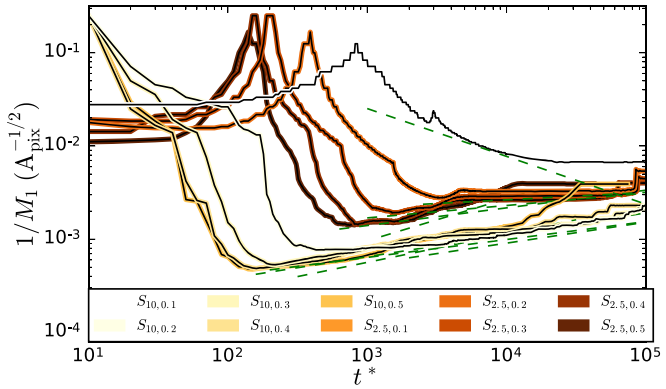

Figure 6. Scaling behavior of $1/M_1 \propto L$ reveal power law domain growth $L \propto t^{*\alpha}$ after spinodal decomposition. Different sphere radii R and mixture parameters x are color coded. Their values are indicated in the legend by $\mathcal{S}^2_{R/R^2_{\square},x}$. $\mathcal{S}^2$ denotes the two-dimensional sphere. As a guide to the eye power-law fits are presented as green dashes lines. They are shifted in a parallel fashion (by multiplication with the factor 0.8) to enhance visibility.

cannot be observed for the small sphere, where the slope changes rapidly from its zero value in the beginning to a high value in the initial nucleation phase of the spinodal decomposition. (M_1 shows the same behavior, shown in the supplementary material.)

In comparison to the power spectrum measure presented in figure 3, the MF graphs are not as smooth since they are more sensitive to dynamical changes in the structure of density profiles. This allows the MFs to detect features of the demixing process that is not accessible via power spectrum analysis. The MFs resolve three distinct phases in the early stage of spinodal decomposition with different domain growth rates: (1) prior to the spinodal decomposition, (2) initial spinodal decompostion, (3) main spinodal decomposition. None of these stages can be detected with the standard demixing metric $L(t)$ obtained by the position of the maximum of the power spectral density as can be seen in figure 3. When plotting the maximum of the angular power spectrum $C_{l,\mathrm{max}}$ phases (1) and (2) can also be detected. (Shown in the supplementary material.) Thus, the maximum of the power spectral density is, in contrast to measures obtained by its position, able to detect the density fluctuation growth characteristic to the spinodal decomposition in the early stage of demixing.

The dynamical range of the MFs depends only on the resolution of the data, since one can always find a threshold value, such that the minimal number of active pixels is close to one. The upper limit is determined by the number of active pixels after spinodal decomposition which scales with the resolution of the data. The power spectrum analysis does not show such a resolution dependence that provides a higher dynamical range proportional to the resolution. For the power spectral density a higher resolution only provides further modes l.

4.4. Characteristic length scale L

Since the MF $M_\nu(K)$ are homogeneous function of order $D - \nu$ (equation (11)) one can expect a scaling behavior of the MFs for the scaling length L:

Table 1. Power-law exponent α during domain growth phase for the large sphere $R = 10R_{11}$. Values are obtained via linear fits in the log–log plots in figures 3 and 6 for $t^* > t_c^*$.

$10000 \cdot \alpha$ for $R = 10R_{11}$	$(2l+1)C_{l,\max}$	L_{PS}	$1/M_1$	$1/\sqrt{M_2}$
$x = 0.1$	—	6221 ± 23	—	—
$x = 0.2$	2240 ± 24	2155 ± 24	2245 ± 13	2178 ± 13
$x = 0.3$	2304 ± 23	2321 ± 27	1921 ± 12	1651 ± 19
$x = 0.4$	2676 ± 28	2531 ± 28	2351 ± 14	2069 ± 26
$x = 0.5$	2190 ± 57	2897 ± 38	3052 ± 21	946 ± 47

Table 2. Power-law exponent α during domain growth phase for the small sphere $R = 2.5R_{11}$. Values are obtained via linear fits in the log–log plots in figures 3 and 6 for $t^* > t_c^*$.

$10000 \cdot \alpha$ for $R = 2.5R_{11}$	$(2l+1)C_{l,\max}$	L_{PS}	$1/M_1$	$1/\sqrt{M_2}$
$x = 0.1$	—	—	—	—
$x = 0.2$	—	1320 ± 160	792 ± 29	1200 ± 210
$x = 0.3$	—	—	1330 ± 30	1000 ± 200
$x = 0.4$	—	1500 ± 30	1894 ± 32	2230 ± 210
$x = 0.5$	3254 ± 38	4511 ± 19	3052 ± 21	—

$$M_0 \propto 1, \quad M_1 \propto L^{-1}, \quad M_2 \propto L^{-2}, \tag{12}$$

L can be interpreted as the characteristic size of demixed domains. Note that L can of be defined via different methods, e.g. as the first zero crossing of the correlation function or as the first moment of the wavelength distribution [10, 11]. These widely used methods are, however, computationally expensive [13]. The scaling behavior of $1/M_1 \propto L$ is presented in figure 6. (For the plot of $1/\sqrt{M_2} \propto L$ consult the supplementary material.) It evidences the power law growth of domain size $L \propto t^{*\alpha}$ during the coalescence phase after spinodal decomposition. The transition from spinodal decomposition to coalescence happens at about $t_c^* \simeq 2 \times 10^2$ in the case of $R = 10R_{11}$ and $t_c^* \simeq 2 \times 10^3$ in the case of $R = 2.5R_{11}$.

For the small sphere only few disjoint domains exist and thus only few coalescence events happen where L changes rapidly. The power law can however still be detected via the mean slope in $1/M_1$. For $1/\sqrt{M_2}$ the few coalescence events result in non-smooth graphs resulting in poor linear fits.

Power-law exponents α obtained by linear fits to the domain growth stages ($t^* > t_c^*$) in figures 3 and 6 are presented in table 1 for the large sphere and respectively in table 2 for the small sphere. Also the fit values for the power spectrum measures, the total power $(2l+1)C_{l,\max}$ and the average domain size L_{PS} are presented. Uncertainties are given by the fit routine. Statistics generally are better for the MFs, in particular $1/M_1$ gives the smallest statistical errors and provides the most comparable curves to a power-law. The angular power spectral density based measures have high uncertainties and in particular for the small sphere they only provide few curves that allow for a power-law fit.

The power-law exponents are found to be close to $\alpha \simeq 0.2$. This is close to the predicted value in [42]. It is smaller than the value of $1/3$ that is predicted in the diffusive domain growth regime of the Lifshitz–Slyozov growth law [29, 43]. Only in the case of the mixture parameter $x = 0.5$ the power-law exponent gets close to the prediction in the diffusive regime.

4.5. Hints towards universal behavior

Motivated by findings in [3] universal features in the demixing behavior on spherical geometries are investigated. We hypothesize that the temporal development of the structure parameters becomes independent of the mixture parameter and sphere size by a suitable rescaling of axis. The rescaled time t_r^* is a function $t_r^* = f(t^*, x, R)$ and the rescaled measures m_r are transformed via $m_r = g(M, x, R)$ for different measures M. The specific scalings are obtained by empirically testing simple functions f and g. In order to remove possible scaling effects due to the mixture parameter x and the sphere size R, that influence the otherwise universal dynamics, the simplest rescaling functions are products of the form $f(t^*, x, R) = t^* x^{\omega} (R/R_{11})^{\Omega}$ and $g(M, x, R) = M x^{\sigma} (R/R_{11})^{\Sigma}$ with real exponents $\omega, \Omega, \sigma, \Sigma \in \mathbb{R}$. We find universal behavior for the MFs M_0 and M_1. This is presented in figure 7 where, after rescaling, the graphs for M_0 and M_1 coincide well for all sphere sizes and mixture parameters $x > 0.1$. The time axis was scaled by $t^* \to t^* \cdot x^{-2/3} \cdot (R/R_{11})^{3/2}$. M_0 was scaled by the mixture parameter as $M_0 \to M_0/x$ in figure 7(b). M_1 was scaled by the mixture parameter and the sphere Radius as $M_1 \to M_1/\sqrt{x}/(R/R_{11})^{0.8}$ in figure 7(c). This hints towards a universal demixing behavior for these systems. Only the graphs for $x = 0.1$ show a different behavior due to their very late start of the demixing process

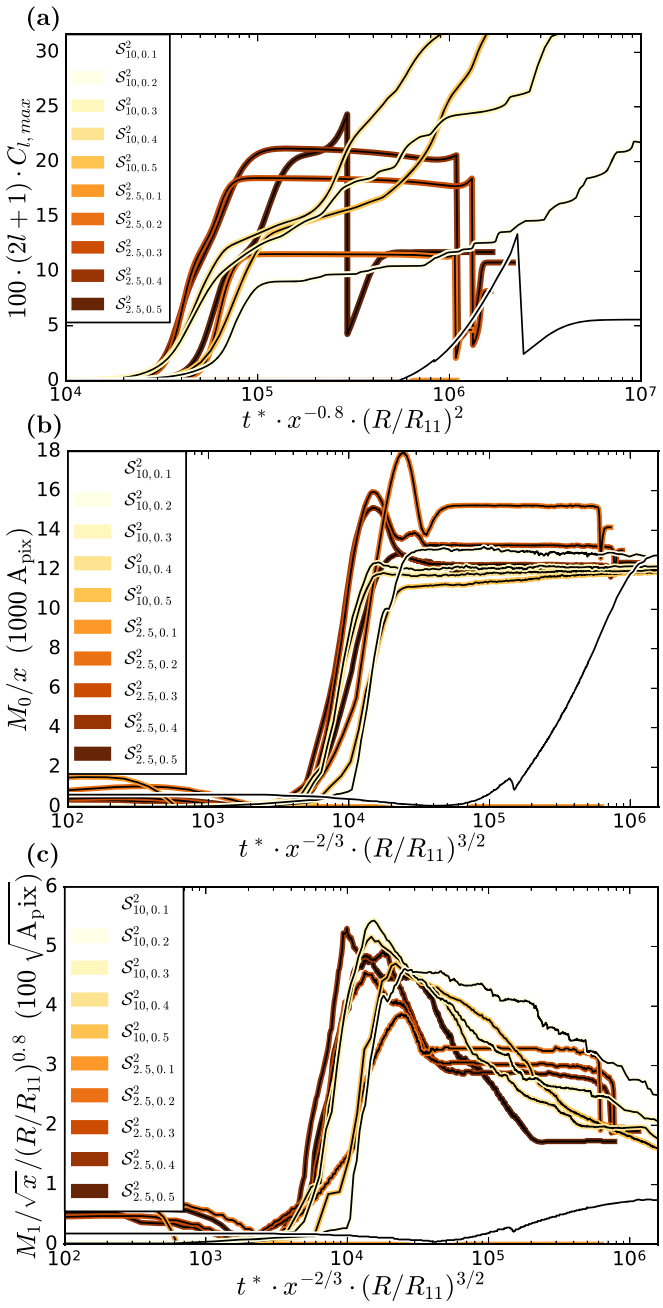

Figure 7. After a rescaling of axis hints of universal behavior are found in panel (b) for M_0 and in panel (c) for M_1. However, in panel (a), no universal behavior is found for power spectral density $(2l+1) \cdot C_{l,\max}$. Different sphere radii R and mixture parameters x are color coded. Their values are indicated in the legend by $\mathcal{S}^2_{R/R^2_{11},x}$. $\mathcal{S}^2$ denotes the two-dimensional sphere.

and thus may have qualitatively different demixing behavior. The specific scaling of axis is obtained by empirical testing of simple functions.

For the power spectral measures no rescaling of the axis could be found that leads to uniform graphs, see figure 7(a). Since this could easily be achieved via MF measures this suggests that nonlinear properties play a role in the demixing process and that hence nonlinear measures, such as the MFs, are a more suitable means for the analysis of demixing processes.

5. Conclusion and outlook

An angular power spectrum analysis for DDFT calculations of the demixing processes on a sphere is able to detect different stages in the demixing process: the onset of spinodal decomposition, the main spinodal decomposition stage and the coalescence stage after spinodal decomposition. A scale-free power law growth $L \propto t^{\alpha}$ could be found for the domain size of demixed domains in the coalescence stage. The onset of the main

spinodal decomposition phase is much later on the small sphere with $R = 2.5R_{11}$ compared to the large sphere with $R = 10R_{11}$. The same behavior is found for the crossover time between spinodal decomposition and coalescence. Also the mixture parameter x influences these times: smaller x shifts the onset of the spinodal decomposition and also the crossover time to coalescence to later times. In the large sphere case many nucleation sites in the spinodal decomposition phase provide a large number of initially demixed domains. Thus during the growth and coalescence phase the domain size power law yields a smooth function. However, in the small sphere case only few nucleation sites exist and therefore also only few initially demixed domains exist after spinodal decomposition and prior to coalescence. This leads to a worse statistic in detecting the domain growth power law in the case of the small sphere.

The main spinodal decomposition stage cannot be detected with the standard method of analyzing the average domain size L_{PS} provided by the structure factor $S(l,\ t)$. This measure is only responsive to the domain coalescence in the late stage of demixing. Using the maximum of the structure factor, the power $(2l + 1)C_{l,\max}$, one can observe the spinodal decomposition stage prior to the coalescence of domains. The MFs provide even further insight: they reveal that the main spinodal decomposition stage actually is composed of two parts: at first the functional measures M_0 and M_1 show a slow growth and after a specific value start to grow faster until the beginning of the coalescence stage. MFs are able to resolve a further level of detail in the spinodal decomposition process. A systematic evaluation of the MFs on further demixing systems might shed new light on the early stage spinodal decompostion dynamics.

Another advantage of MFs is their scaling behavior during the coalescence stage: The domain growth power-laws are reproduced with higher precision than using the angular power spectrum method. The MFs seem to be a convenient measure to efficiently determine domain growth power-law exponents and shed light on a possible connection between the growth rate and the domain morphology.

The MFs allow the precise measurement of the mixture parameter x only observing the early stage spinodal decomposition without knowledge of the demixed end state. Since the density in the initial mixture is $\rho/\rho_{\mathrm{th},100} \simeq x$, all relative threshold values below x result in almost no pixels being active after binarization, but almost all pixels are active for higher thresholds. This leads to a sharp transition of the value of the MFs at $\rho_{\mathrm{th}}/\rho_{\mathrm{th},100} \simeq x$.

The most interesting new insight gained by a morphological MF analysis is their universal behavior. By applying a suitable rescaling, all MFs collapse onto a single master curve. The only exception being the curve for the smallest mixture parameter $x = 0.1$, suggesting a qualitatively different demixing scenario with a much later onset of phase separation. For higher mixture parameters this shows that the analyzed demixing process has a universal, parameter independent domain evolution. For the angular power spectrum measures no suitable rescaling of the axis could be found. This suggests that nonlinear properties play an important role in the demixing process and thus that the inherently nonlinear MFs are a suitable tool for the characterization of this process. In further studies we will use surrogates [17–19] in order to disentangle the linear and nonlinear effects of the demixing process and their impact on the behavior of the MFs.

This result immediately suggest further analysis of the binary demixing system on spherical geometry: What are the differences between the low and high mixture parameter classes and how is the transition between these classes? Other questions worth of further examination are: Is this behavior influenced by the interaction potential, and is there a connection to the flat three-dimensional case?

Hints towards universal behavior in demixing systems via MF (and tensor) analysis were already discovered in previous studies [3]. Here simulations of a three-dimensional system with a binary complex plasma were analyzed. A universal behavior was found for different screening length rations of a double Yukawa interaction potential. There, also an exception of the universal behavior was found for a single screening length interaction potential. Further investigation of the universal behavior of demixing processes on various geometries, boundary conditions and with various interaction potentials are vital in order to obtain a thorough understanding of the fundamental properties of demixing systems. The preliminary analyses in this work and in [3] suggest that further investigation will lead to deeper insight into the physical mechanisms of the demixing of binary systems.

Applying higher ranked (tensor) Minkowski valuations to demixing DDFT calculations on spherical geometries in further studies may shed further light on the features of the universal properties of the demixing process. Tensor MF on the two-sphere $\mathcal{S}^2$ were introduced and applied in [44, 45]. Higher ranked Minkowski tensor measures already proved to be useful in characterizing the solid–liquid phase transition in a two-dimensional flat complex plasma [46]. Also the resolution of the DDFT calculations can be significantly improved in further studies.

This study gives further evidence that MF methods are a powerful tool for morphological characterization of physical processes. They are superior to conventional analysis methods in various respects: they directly provide information on the morphology of structures, are inherently nonlinear, and are fast and easy to compute (by only counting pixels) compared to correlation function measures. They allow the measurement of the

characteristic length scale L with high statistical reliability even for low resolution data. MF analysis is able to quickly reveal new aspects of interest in particular in nonlinear (non-Gaussian) data. It is founded on a solid mathematical framework, however it still provides easily interpretable results.

Acknowledgments

We thank I Laut for carefully checking this manuscript. AB was funded by the StMWi, MCB acknowledges funding provided by the Swiss National Science Foundation through the National Center of Competence in Research Bio-Inspired Materials.

ORCID iDs

A Böbel https://orcid.org/0000-0001-5612-7543

References

[1] Gunton J D, Miguel M and Sahni P S 1983 The dynamics of first order phase transitions *Phase Transitions and Critical Phenomena* ed C Domb and J Lebowitz (New York: Academic)
[2] Bray A J 1994 *Adv. Phys.* **43** 357–459
[3] Böbel A and Räth C 2016 *Phys. Rev.* E **94** 013201
[4] Li W H and Lee J 1994 *Phys. A: Stat. Mech. Appl.* **202** 165–74
[5] Lee J 1994 *Phys. A: Stat. Mech. Appl.* **210** 127–38
[6] Bott M C and Brader J M 2016 *Phys. Rev.* E **94** 012603
[7] Guerra R E, Kelleher C P, Hollingsworth A D and Chaikin P M 2018 *Nature* **554** 346
[8] Soni V, Gómez L R and Irvine W T M 2018 *Phys. Rev.* X **8** 011039
[9] Krause A L, Burton A M, Fadai N T and Van Gorder R A 2018 *Phys. Rev.* E **97** 042215
[10] Stanley H E 1987 *Introduction to Phase Transitions and Critical Phenomena* (Oxford: Oxford University Press)
[11] Allen M P and Tildesley D J 1987 *Computer Simulation of Liquids* (New York: Oxford University Press)
[12] Wysocki A *et al* 2010 *Phys. Rev. Lett.* **105** 045001
[13] Velasco E and Toxvaerd S 1996 *Phys. Rev.* E **54** 605–10
[14] Mecke K R and Sofonea V 1997 *Phys. Rev.* E **56** R3761–4
[15] Sofonea V and Mecke K 1999 *Eur. Phys. J.* B **8** 99–112
[16] Minkowski H 1903 *Math. Ann.* **57** 447–95
[17] Rossmanith G, Modest H, Räth C, Banday A J, Górski K M and Morfill G 2012 *Phys. Rev.* D **86** 083005
[18] Modest H I, Räth C, Banday A J, Rossmanith G, Sütterlin R, Basak S, Delabrouille J, Górski K M and Morfill G E 2013 *Mon. Not. R. Astron. Soc.* **428** 551–62
[19] Modest H I, Räth C, Banday A J, Górski K M and Morfill G E 2014 *Phys. Rev.* D **89** 123004
[20] Stillinger F H 1976 *J. Chem. Phys.* **65** 3968
[21] Archer A J and Evans R 2001 *Phys. Rev.* E **64** 041501
[22] Louis A A, Bolhuis P G and Hansen J P 2000 *Phys. Rev.* E **62** 7961–72
[23] Archer A J and Evans R 2004 *J. Chem. Phys.* **121** 4246–54
[24] Marconi U M B and Tarazona P 1999 *J. Chem. Phys.* **110** 8032
[25] Driscoll J and Healy D 1994 *Adv. Appl. Math.* **15** 202–50
[26] Onuki A 2002 *Phase Transition Dynamics* (Cambridge: Cambridge University Press)
[27] https://healpy.readthedocs.io
[28] Górski K M, Hivon E, Banday A J, Wandelt B D, Hansen F K, Reinecke M and Bartelmann M 2005 *Astrophys. J.* **622** 759
[29] Thakre A K, den Otter W K and Briels W J 2008 *Phys. Rev.* E **77** 011503
[30] Furukawa H 1984 *Phys. A: Stat. Mech. Appl.* **123** 497–515
[31] Weil W 1983 *Stereology: A Survey for Geometers* (Basel: Birkhäuser Basel) pp 360–412
[32] Schneider R 2013 Convex bodies: the Brunn-Minkowski theory *Encyclopedia of Mathematics and its Applications* 2nd edn (Cambridge: Cambridge University Press)
[33] Mecke K R, Buchert T and Wagner H 1994 *Astron. Astrophys.* **288** 697–704
[34] Hadwiger H 1957 *Vorlesungen über Inhalt, Oberfläche und Isoperimetrie* (Berlin: Springer)
[35] Helfrich W 1973 *Z. Naturforsch.* **28c** 693–703
[36] Mecke K R 1996 *Phys. Rev.* E **53** 4794–800
[37] Rosenfeld Y 1995 *Mol. Phys.* **86** 637–47
[38] Mecke K 2000 Additivity, convexity and beyond: applications of Minkowski functionals in statistical physics *Statistical Physics and Spatial Statistics* (*Lecture Notes in Physics* vol 554) ed K R Mecke and Stoyan D S (Berlin: Springer) pp 111–84
[39] Schmalzing J and Górski K M 1998 *Mon. Not. R. Astron. Soc.* **297** 355–65
[40] Winitzki S and Kosowsky A 1998 *New Astron.* **3** 75–99
[41] Michielsen K and Raedt H D 2001 *Phys. Rep.* **347** 461–538
[42] Binder K and Stauffer D 1974 *Phys. Rev. Lett.* **33** 1006–9
[43] Lifshitz I and Slyozov V 1961 *J. Phys. Chem. Solids* **19** 35–50
[44] Chingangbam P, Yogendran K, Joby P, Ganesan V, Appleby S and Park C 2017 *J. Cosmol. Astropart. Phys.* **2017** 023
[45] Ganesan V and Chingangbam P 2017 *J. Cosmol. Astropart. Phys.* **2017** 023
[46] Böbel A, Knapek C A and Räth C 2018 *Phys. Rev.* E **97** 053201